

# The finite-element method for the propagation of light in scattering media: Frequency domain case

M. Schweiger<sup>a)</sup>

*Department of Medical Physics and Bioengineering, University College London, Capper Street, London WC1E 6JA, England*

S. R. Arridge

*Department of Computer Science, University College London, Gower Street, London WC1E 6BT, England*

(Received 7 February 1996; accepted for publication 15 March 1997)

A frequency domain light transport model to simulate the transillumination of a scattering object with radio frequency intensity modulated light is presented. The model is based on the diffusion approximation to the radiative transfer equation and uses a finite-element model to allow for complex geometries and an inhomogeneous distribution of absorption and scattering. It calculates the complex photon density within the object and the complex exitance on the boundary of the object. The model is validated against an analytic Green's function model for a circular geometry in the homogeneous case, and its accuracy is investigated for a range of mesh resolutions, optical parameters, and modulation frequencies. © 1997 American Association of Physicists in Medicine. [S0094-2405(97)00606-8]

Key words: diffusion equation, frequency domain, finite-element method

## I. INTRODUCTION

In recent years the transillumination of tissue with light in the optical and near-infrared wavelength range has received widespread attention. Transillumination systems in general work by irradiating a point on the surface of the body, and measuring the boundary fluence (exitance) at other surface points. They can be divided into three different categories: continuous wave systems for measuring the stationary exitance, time-resolved systems for measuring the temporal distribution of the exitance caused by an ultrashort input pulse, and frequency systems which use an intensity modulated source and measure the phase shift and modulation depth of the detected signal.

It can be shown that the information content of measurements in the frequency domain, sampled at all wavelengths, is equivalent to that of temporal data, sampled at all times.<sup>1</sup> In practice, frequency systems are easier and cheaper to manufacture than time-domain systems which need sophisticated ultrashort pulse lasers and highly time-resolved detectors.<sup>2</sup> It is therefore expected that frequency systems will become the method of choice in commercial transillumination devices. Various prototypes have been built to date for spectroscopic and imaging applications and are currently used in clinical trials.<sup>3,4</sup>

In general it will be sufficient to take measurements at a single or a few wavelengths. In the time domain this corresponds to compressing the data set by extracting certain characteristic statistical properties such as the integrated intensity, mean time of flight, and higher moments from the temporal profile.

For both imaging and spectroscopic applications the availability of an accurate, fast, and versatile light transport model is essential. For spectroscopy, such a model can be used to predict the probed region for a given distribution of

the optical properties inside the body, and given positions of the source and measurement positions. This is particularly important for highly inhomogeneous tissues like the head where the light distribution is strongly distorted.<sup>5</sup> In image reconstruction algorithms which employ an iterative approach the light transport model is used as a forward model for generating data from the image at each iteration step.

We have previously presented a light transport model based on the diffusion approximation to the transport equation for calculating either the full temporal profile of the exitance,<sup>6</sup> or directly the integrated exitance, mean time of flight, and higher moments.<sup>7</sup> Our approach uses the finite-element method (FEM) to allow the modeling of complex geometries and inhomogeneous distribution of absorption and scattering coefficients.

In this paper we extend this model to handle frequency-domain problems. We derive the complex FEM formulation from the Fourier transform of the temporal diffusion equation, discuss specific problems of the implementation, and validate the model against results from an analytic Green's function model for a variety of parameters.

## II. DIFFUSION MODEL

The light transport model considered in this paper is the diffusion approximation to the radiative transfer equation. The validity of this approach has been shown in numerous papers,<sup>8-10</sup> if the prerequisites for the assumption of diffuse light transport are met. The diffusion approximation is valid for scatter-dominated light propagation, away from sources and boundaries. Despite the latter condition, we and various other authors have shown that the diffusion approximation allows quantitative predictions of boundary measurements.<sup>6,11,12</sup> For a more detailed discussion of the derivation

of the diffusion model and its range of validity we refer the reader to the previous two papers in this series.<sup>6,13</sup>

The diffusion equation in the temporal domain for the photon density  $\Phi(\mathbf{r}, t)$  at a point  $\mathbf{r} \in \Omega$  inside a scattering domain  $\Omega$ , bounded by  $\partial\Omega$ , is given by

$$\frac{1}{c} \frac{\partial \Phi(\mathbf{r}, t)}{\partial t} - \nabla \cdot \kappa(\mathbf{r}) \nabla \Phi(\mathbf{r}, t) + \mu_a(\mathbf{r}) \Phi(\mathbf{r}, t) = q_0(\mathbf{r}, t), \quad (1)$$

where  $\mu_a$  and  $\mu_s$  are the absorption and scattering coefficients,  $\kappa(\mathbf{r}) = \{3[\mu_a(\mathbf{r}) + \mu'_s(\mathbf{r})]\}^{-1}$  is the diffusion coefficient,  $\mu'_s = (1 - \bar{f})\mu_s$  is the reduced scattering coefficient,  $\bar{f}$  is the anisotropy factor of the single scattering angle distribution,  $c = c_0/n$  is the speed of light in the medium with refractive index  $n$ , and  $q_0$  is an isotropic source distribution. The measured quantity is the photon current through the boundary (exitance)  $\Gamma(\xi)$  at some point  $\xi \in \partial\Omega$ . The relation between  $\Phi$  and  $\Gamma$  is given by Fick's law,

$$\Gamma(\xi, t) = -c\kappa(\xi) \nabla_n \Phi(\xi, t), \quad (2)$$

where  $\nabla_n$  is the derivative in the direction of the outward normal to the boundary at  $\xi$ .

In this paper we assume the input source to be a collimated pencil beam incident at  $\zeta \in \partial\Omega$ . The standard way to simulate this situation in a diffusion model is to represent the source by a diffuse point source at a point  $\mathbf{r}_s$  one mean scattering length beneath  $\zeta$ ,<sup>14</sup>

$$q_0(\mathbf{r}, t) = \delta(\mathbf{r} - \mathbf{r}_s) Q(t), \quad (3)$$

where  $Q(t)$  is the source strength.

In the frequency domain the input signal  $Q$  is modulated with a frequency  $f = \omega/2\pi$ ,

$$Q(\omega) = Q_0 + A^{(S)} e^{i\omega t}, \quad (4)$$

where  $Q_0$  is the average intensity and  $A^{(S)}$  is the modulation amplitude of the source. At a measurement site  $\xi$  the detected current  $\hat{\Gamma}$  is then given by

$$\hat{\Gamma}(\xi, \omega) = \Gamma_0(\xi) + A^{(\Gamma)}(\xi) e^{i[\omega t + \varphi(\xi)]}. \quad (5)$$

To obtain  $\hat{\Gamma}$  we use the Fourier transform of Eq. (1),

$$\begin{aligned} \frac{1}{c} i\omega \hat{\Phi}(\mathbf{r}, \omega) - \nabla \cdot \kappa(\mathbf{r}) \nabla \hat{\Phi}(\mathbf{r}, \omega) + \mu_a(\mathbf{r}) \hat{\Phi}(\mathbf{r}, \omega) \\ = \hat{q}_0(\mathbf{r}, \omega), \end{aligned} \quad (6)$$

where  $\hat{\Phi}$  is the complex photon density. The dc component of Eq. (5),  $\Gamma_0$ , is obtained by finding the steady-state photon density  $\Phi_0$  from Eq. (6) with  $\omega=0$ , and inserting this into Eq. (2). The ac component,  $\hat{\Gamma}^{(\text{ac})} = A^{(\Gamma)} e^{i(\omega t + \varphi)}$  is obtained by solving Eq. (6) for a given  $\omega$  and applying Fick's law in frequency domain,

$$\hat{\Gamma}^{(\text{ac})}(\xi, \omega) = -c\kappa(\xi) \nabla_n \hat{\Phi}(\xi, \omega). \quad (7)$$

The quantities measured in an experiment will be the phase shift  $\varphi$  between source and measurement signal,

$$\varphi(\xi) = \arg \Gamma^{(\text{ac})}(\xi, \omega) = \tan^{-1} \frac{\text{Im} \Gamma^{(\text{ac})}(\xi, \omega)}{\text{Re} \Gamma^{(\text{ac})}(\xi, \omega)}, \quad (8)$$

and the modulation amplitude  $A^{(\Gamma)}$  of the measurement signal,

$$A^{(\Gamma)}(\xi, \omega) = \text{mod} \Gamma^{(\text{ac})}(\xi, \omega) = |\Gamma^{(\text{ac})}(\xi, \omega)|. \quad (9)$$

For convenience we normalize  $A$  to obtain the modulation depth,

$$m(\xi, \omega) = \frac{A^{(\Gamma)}(\xi, \omega)}{\Gamma_0(\xi)}. \quad (10)$$

The boundary conditions used in this paper are based on an extrapolated boundary method which has been described in detail for the time-domain case in part 2 of this series.<sup>13</sup> This works by applying a Dirichlet condition  $\hat{\Phi}(\xi, \omega) = 0 \forall \xi \in \partial\Omega'$ , where  $\partial\Omega'$  is a virtual boundary at a distance  $d_{\text{ext}}$  beyond  $\partial\Omega$ . In the case of a refractive index mismatch, an expression for  $d_{\text{ext}}$  is given by Moulton,<sup>15</sup>

$$d_{\text{ext}} = \sqrt{\frac{\kappa}{\mu_a}} \tanh^{-1}(2R \sqrt{\kappa \mu_a}), \quad (11)$$

where  $R$  is a term incorporating internal reflections at the tissue-air interface due to a refractive-index mismatch.<sup>16</sup> A refractive index of  $n=1.4$  produces  $R=2.74$ . We have shown this method to be equivalent to a Robin-type boundary condition,<sup>13</sup> which in the frequency domain is given by

$$\hat{\Phi}(\xi, \omega) - 2\kappa(\xi) R \nabla \hat{\Phi}(\xi, \omega) = 0 \forall \xi \in \partial\Omega. \quad (12)$$

### III. FINITE ELEMENT CALCULATIONS

To discretize Eq. (6) we use a Galerkin approach which for the time-domain problem [Eq. (1)] has been described previously.<sup>6</sup> This proceeds by dividing the domain  $\Omega$  into a mesh of  $D$  triangular elements, joined at  $P$  nodes, and defining a piecewise linear approximation  $\hat{\Phi}^h$  to  $\hat{\Phi}$  in terms of a set of linear basis functions  $\psi_j$ ,  $j=1, \dots, P$  with limited support. The discrete formulation of Eq. (6) can be written as

$$[\mathbf{K}(\kappa) + \mathbf{C}(\mu_a) + i\omega c^{-1} \mathbf{B}] \hat{\Phi}(\omega) = \hat{\mathbf{Q}}(\omega), \quad (13)$$

where the complex vectors  $\hat{\Phi}$  and  $\hat{\mathbf{Q}}$  represent the nodal solution and source values, respectively, and  $\mathbf{K}$ ,  $\mathbf{C}$ ,  $\mathbf{B} \in \mathbb{R}^{P \times P}$  are system matrices.<sup>6</sup>

Boundary conditions are imposed by adding an additional layer of elements around the mesh, whose thickness is given by Eq. (11), and forcing the solution at the nodes of the extrapolated boundary to zero.

The complex matrix equation (13) is of the form  $\hat{\mathbf{Z}}(\omega) \hat{\Phi}(\omega) = \hat{\mathbf{Q}}_0(\omega)$ ,  $\hat{\mathbf{Z}} \in \mathbb{C}^{P \times P}$ ,  $\hat{\Phi}, \hat{\mathbf{Q}} \in \mathbb{C}^P$ . We convert this into the equivalent real  $\mathbb{R}^{2P \times 2P}$  problem of the form

$$\begin{pmatrix} \text{Re} \hat{\mathbf{Z}} & -\text{Im} \hat{\mathbf{Z}} \\ \text{Im} \hat{\mathbf{Z}} & \text{Re} \hat{\mathbf{Z}} \end{pmatrix} \begin{pmatrix} \text{Re} \hat{\Phi} \\ \text{Im} \hat{\Phi} \end{pmatrix} = \begin{pmatrix} \text{Re} \hat{\mathbf{Q}} \\ \text{Im} \hat{\mathbf{Q}} \end{pmatrix}. \quad (14)$$

Once Eq. (14) has been solved by the method described below, the complex exitance  $\hat{\Gamma}(\xi, \omega)$  at a point  $\xi \in \partial\Omega$  can be calculated with Eq. (7), and subsequently the measurement quantities  $m(\xi, \omega)$  and  $\varphi(\xi, \omega)$ .

We have mentioned previously<sup>6</sup> that the FEM discretization of the lossy diffusion equation requires a high mesh

resolution to guarantee sufficient accuracy, leading typically to a number of nodes of the order  $P \approx 10^4$  for two-dimensional (2D) problems and  $P \approx 10^5 - 10^6$  for three-dimensional (3D) problems. This makes the use of sparse matrix techniques imperative. First, memory requirements can be halved by storing only one copy of both  $\text{Re } \hat{\mathbf{Z}}$  and  $\text{Im } \hat{\mathbf{Z}}$ , and adding some additional bookkeeping during the solution of Eq. (14). Both  $\text{Re } \hat{\mathbf{Z}}$  and  $\text{Im } \hat{\mathbf{Z}}$  are sparse, with nonzero elements  $Z_{ij}$  only for such nodes  $i$  and  $j$  which share a common element. With the geometry employed, for 2D problems the number of nonzero elements per row is typically about 7, for 3D problems about 21. Exploiting this property with a sparse matrix representation reduces the system matrix memory size by a factor of order  $10^3 - 10^4$ . This is a significantly higher compression than the band matrix representation we use for the time-domain model.

The sparse matrix scheme can in principle also be used in the time domain when memory efficiency is of importance. However, this aggravates the use of the fast Cholesky matrix solver, due to fill-in in the reduction step. In the frequency case this is not relevant as the nonsymmetry of the matrix prevents the application of the Cholesky solver.

Instead we use an iterative conjugate gradient (CG) scheme. This has the advantage of accessing  $\hat{\mathbf{Z}}$  only for matrix-times-vector type operations, which can be coded very efficiently for sparse matrices.<sup>17,18</sup> To improve the convergence rate the diagonal of  $\hat{\mathbf{Z}}$  is used as a preconditioner. The iteration is terminated when the norm of the residual levels out. Typically about  $\sqrt{P}$  iterations are required. The optimized CG algorithm is roughly a factor of 2–5 faster than the Cholesky decomposition plus forward/backward substitution, but a factor of 10 slower than the forward/backward substitution alone. This is of importance when multiple sources are considered, as will be the case in a tomographic reconstruction setup, since the Cholesky scheme requires only a single decomposition for a given mesh, regardless of the number of sources, while the CG solution must be repeated for each source. A short overview of Cholesky and CG schemes is given in the Appendix.

#### IV. ANALYTIC REFERENCE MODEL

An analytic solution of the diffusion equation in frequency domain is used to calculate the discretization error of the FEM model. Exact solutions for the complex intensity in the homogeneous case are available for a limited number of simple geometries.<sup>1</sup> The Green's function (GF)  $\hat{G}^{(\Phi)}$  for the 2D circle with radius  $a$  is given by

$$\hat{G}^{(\Phi)}(\mathbf{r}, \mathbf{r}_s, \omega, t) = \frac{e^{-i\omega t}}{2\pi c \kappa} \sum_{n=-\infty}^{\infty} \cos(n\theta) \frac{I_n(\alpha r_s)}{I_n(\alpha a')} \times [K_n(\alpha r) I_n(\alpha a') - I_n(\alpha r) K_n(\alpha a')], \quad (15)$$

where  $I_n$  and  $K_n$  are the modified Bessel functions of the first and second kind,  $\mathbf{r}_s$  is the source position,  $\alpha(\omega) = \sqrt{3(\mu_a + \mu'_s)(\mu_a + i\omega c^{-1})}$ , and  $a'$  is the radius of the ex-

TABLE I. FEM meshes used for the calculation of discretization errors.

Mesh	$h/a$	No. elements	No. nodes
CIRC08	0.140	595	324
CIRC16	0.079	1931	1 015
CIRC32	0.042	6912	3 553
CIRC64	0.021	26116	13 251

trapolated circle,  $a' = a + d_{\text{ext}}$ . From Eq. (15) the exitance can be derived by applying Eq. (7). This model uses the same extrapolated boundary condition and source specification as the discrete model, so the results can be compared directly.

#### V. RESULTS AND DISCUSSION

In this section we investigate the stability of the FEM model for a range of parameters, by comparing the results for the boundary measurements  $\varphi$  and  $m$  with those obtained from the analytic model. Simulations are performed on a circle with radius  $a = 25$  mm, and we express the accuracy of the FEM model in terms of the relative error  $\epsilon(\alpha)$  in  $\varphi$  and  $m$ , at the angular spacing  $\alpha$  between source and detector, measured at the center of the circle,

$$\epsilon^{(\varphi)}(\alpha) = |\varphi^{(\text{FEM})}(\alpha) - \varphi^{(\text{GF})}(\alpha)| / |\varphi^{(\text{GF})}(\alpha)|, \quad (16)$$

$$\epsilon^{(m)}(\alpha) = |m^{(\text{FEM})}(\alpha) - m^{(\text{GF})}(\alpha)| / |m^{(\text{GF})}(\alpha)|. \quad (17)$$

The influence of the following parameters on the accuracy of the FEM results is investigated: mesh resolution, error limit of the CG solver, absorption and scattering coefficients  $\mu_a$  and  $\mu'_s$ , refractive index  $n$ , and modulation frequency  $f$ .

As default values we choose  $\mu_a = 0.025 \text{ mm}^{-1}$ ,  $\mu'_s = 2.0 \text{ mm}^{-1}$ ,  $n = 1.4$ , and  $f = 200$  MHz. The default mesh consists of 6912 elements and 3553 nodes, and the default CG error limit  $\rho$  (see the Appendix) is  $10^{-16}$ . In the following we vary each of these parameters consecutively while keeping the others at their default value. In each case we calculate  $\epsilon^{(\varphi)}$  and  $\epsilon^{(m)}$  and plot them both as a function of the angular optode separation and as a function of the tested parameter at an optode spacing of  $90^\circ$ .

The FEM mesh structure is the same as in the time-dependent case and has been described previously.<sup>6,13</sup>

##### A. Discretization and matrix solution errors

The resolution of the mesh plays an important role for the stability and accuracy of the FEM model. To investigate this effect we discretize the circular domain with meshes of different resolution and compare the calculated boundary measurements with the analytic results. The mesh resolution is defined in terms of  $h/a$ , where  $h$  is diameter of the largest element, and  $a$  is the mesh radius. Four different mesh resolutions are used, as listed in Table I. Figure 1(a) shows  $\epsilon^{(\varphi)}$  and  $\epsilon^{(m)}$  as a function of optode separation for the four meshes and Fig. 1(b) shows  $\epsilon^{(\varphi)}(90^\circ)$  and  $\epsilon^{(m)}(90^\circ)$  as a function of  $h/a$ , together with the computer run time, measured on a SPARC 20 workstation. The results show that the

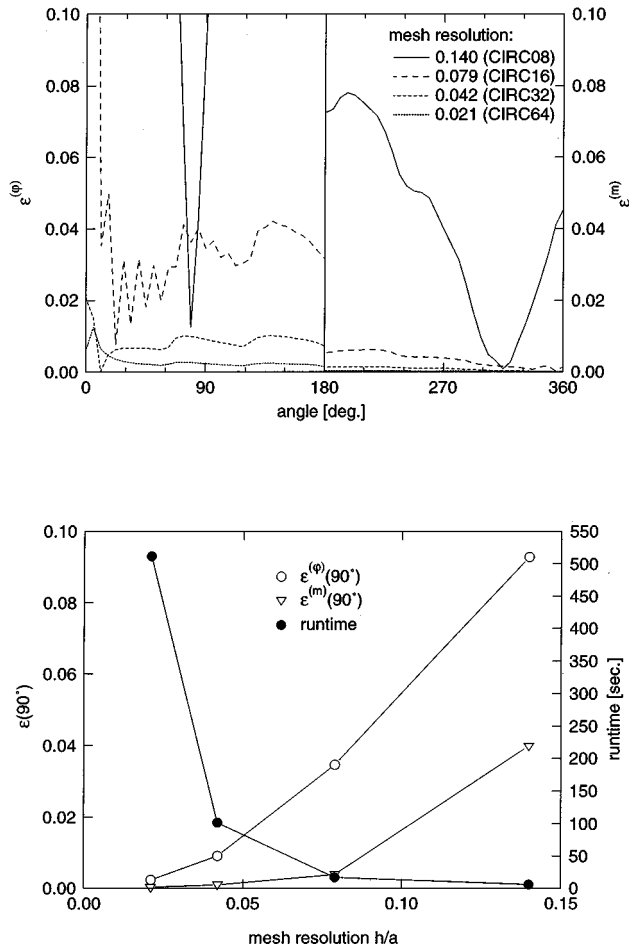


FIG. 1. Discretization error  $\epsilon$  of phase shift and modulation depth for different mesh resolutions; as a function of detector position (top) and as a function of mesh resolution, at detector position  $90^\circ$  (bottom).

FEM discretization error converges toward zero for high mesh resolutions. The error of  $m$  is generally smaller than that of  $\varphi$  for the given parameters. In the following we use CIRC32 as the default mesh, providing a compromise between accuracy and run time, with  $\epsilon^{(\varphi)} < 0.01$  and  $\epsilon^{(m)} < 0.0015$ . The very small error in  $m$  is probably caused by the fact that  $m$  is defined as the ratio [Eq. (10)] which eliminates systematic errors in the solution of the light transport model.

The performance of the FEM model is further affected by the error limit set as a stopping criterion for the CG solver. Figure 2 shows the errors for CG error limits  $\rho$  between  $10^{-4}$  and  $10^{-14}$ . For large error limits the model breaks down, while on the other hand the results do not change below  $\rho = 10^{-12}$ . For smaller error limits the error of the results is dominated by the FEM discretization error. If a higher mesh resolution is chosen to reduce the discretization error, additional CG iterations are required to arrive at the highest achievable accuracy. This demonstrates the necessity to match the CG error limit to the mesh resolution to optimize the quality of the results without wasting computing time.

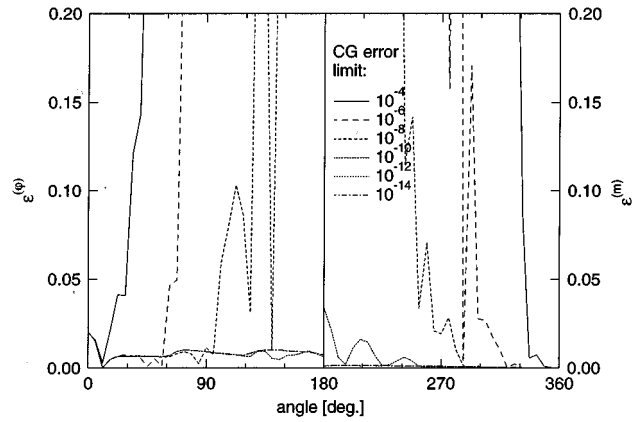


FIG. 2. Discretization error of phase shift and modulation depth for different conjugate gradient error limits. Note that the errors for CG limits  $10^{-12}$  and  $10^{-14}$  are indistinguishable in this graph.

## B. Influence of the optical parameters

The optical parameters  $\mu_a$ ,  $\mu'_s$ , and  $n$  affect the boundary measurements of  $\varphi$  and  $m$ , and also the error of the FEM model in calculating these values. To test this we present simulation results for a physiologically relevant range of absorption, scattering, and refractive index values.

Figure 3(a) shows the values of  $\varphi$  and  $m$  as calculated by the FEM and GF models for different absorption coefficients, as a function of angular optode spacing. As expected, the magnitude of  $\varphi$  decreases, while  $m$  increases, as  $\mu_a$  rises. The error  $\epsilon^{(\varphi)}$  [Fig. 3(b)] increases approximately linearly with  $\mu_a$ , but for all tested absorption values remains below 2%, apart from very small optode spacings  $< 10^\circ$  where the error reaches 3% for  $\mu_a = 0.04 \text{ mm}^{-1}$ .  $\epsilon^{(m)}$  is affected by  $\mu_a$  only to a small extent, and even decreases with increasing  $\mu_a$ . This is confirmed in Fig. 3(c) which shows the errors of  $\varphi$  and  $m$  measured at an optode separation of  $90^\circ$  as a function of  $\mu_a$ .

Figure 4 shows the corresponding graphs for a variation of the scattering coefficient  $\mu'_s$  between  $0.5$  and  $3 \text{ mm}^{-1}$ . The effect of  $\mu'_s$  on the measurements is inverse to that of  $\mu_a$  with higher values leading to an increase of  $|\varphi|$  and a decrease of  $m$  [Fig. 4(a)]. This is analogous to the time domain, where the mean time of flight increases for higher scattering but decreases for higher absorption.<sup>19</sup> The errors  $\epsilon^{(\varphi)}$  and  $\epsilon^{(m)}$  are shown in Figs. 4(b) and 4(c).

Figure 5 shows the effect of a change in the refractive index  $n$  between  $1.0$  and  $1.5$  on the boundary measurements [Fig. 5(a)] and on the FEM errors [Figs. 5(b) and 5(c)]. An increase in  $n$  leads to an increase in  $|\varphi|$  and a decrease in  $m$ . The FEM errors are largely unaffected by a variation of  $n$ .

## C. Influence of modulation frequency

Finally we test the effect of a variation of the modulation frequency  $f$  of the input signal between  $0$  and  $1000 \text{ MHz}$  on the boundary measurements and the accuracy of the FEM model.

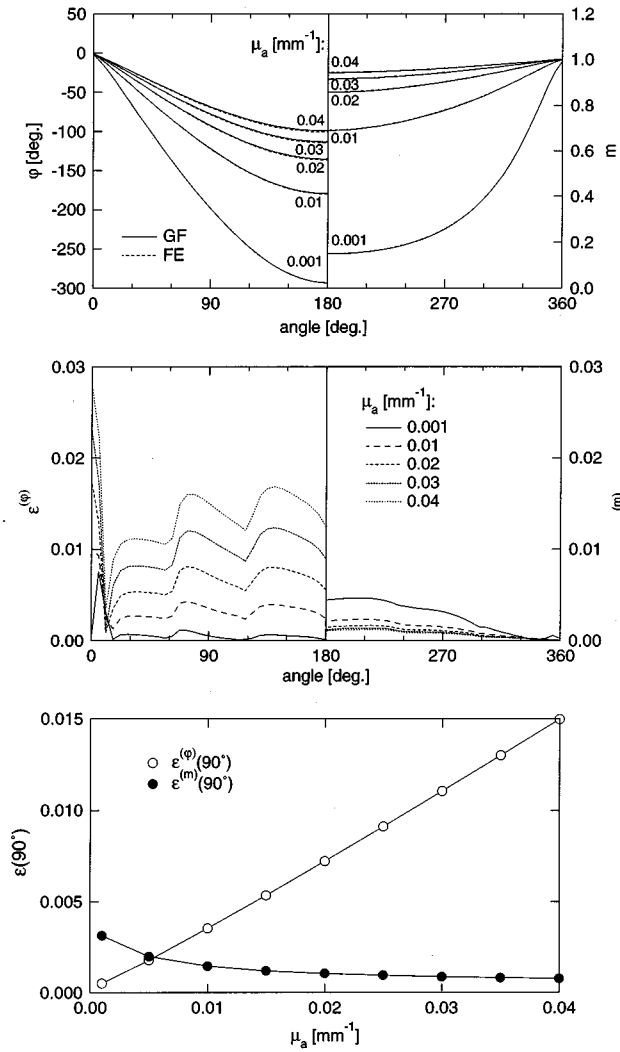


FIG. 3. Boundary measurements and FEM errors for different absorption coefficients. Measurement values as a function of optode spacing (top), error of the FEM model as a function of optode spacing (center) and as a function of  $\mu_a$  at  $90^\circ$  (bottom).

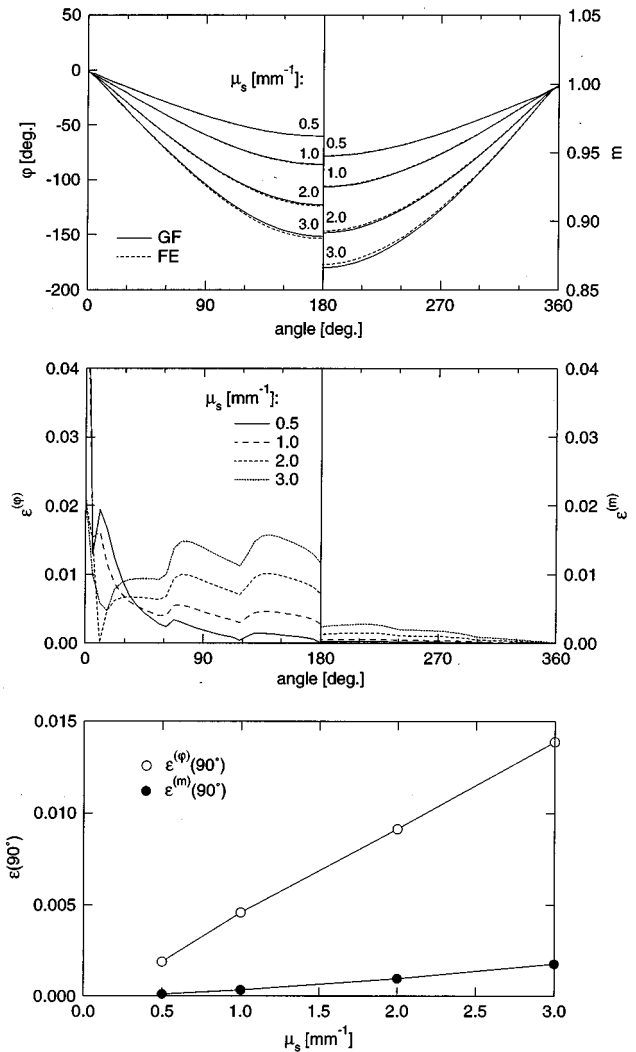


FIG. 4. Boundary measurements and FEM errors for different scattering coefficients. Graphs correspond to Fig. 3.

Figure 6(a) shows the expected relationship between  $f$  and  $\varphi$  and  $m$ , where an increase in  $f$  leads to an increase of  $|\varphi|$  and a decrease of  $m$ . The errors of  $\varphi$  are largely independent of  $f$ , while the error of  $m$  rises significantly with  $f$  [Figs. 6(b) and 6(c)]. This suggests that for a calculation of modulation depth at high modulation frequencies, meshes with a higher resolution than CIRC32 will be required.

**VI. CONCLUSION**

We have developed a light transport model which can be applied to the simulation of frequency-domain transillumination problems. It allows the calculation of the complex intensity, phase shift, and modulation depth at any point of the surface of the object. The model is based on a finite-element solution of the diffusion equation and can be used for irregular geometries and inhomogeneous distributions of the absorption and scattering parameters. It uses an extrapolated boundary method which has previously been shown to agree

well with a Robin-type boundary condition. This also allows the inclusion of refractive-index mismatches at the tissue-air interface.

The frequency-domain case is governed by an elliptic partial differential equation, whereas the time-domain problem discussed previously<sup>6,13</sup> is parabolic. The system matrix in the frequency case is not positive-definite, which prevents the application of the Cholesky matrix solver. To overcome these problems we developed an efficient sparse matrix algorithm in conjunction with a biconjugate gradient solver which allows the use of highly resolved FEM meshes which improves the numerical stability of the model and will in the future allow the solution of 3D problems. We have included a detailed discussion on the error behavior to demonstrate the impact of the choice of model parameters on the accuracy of the results, a topic of particular interest to the medical imaging community.

The FEM model has been tested against an analytic Green's function model for the 2D homogeneous circular problem. We have shown that the numerical stability of the

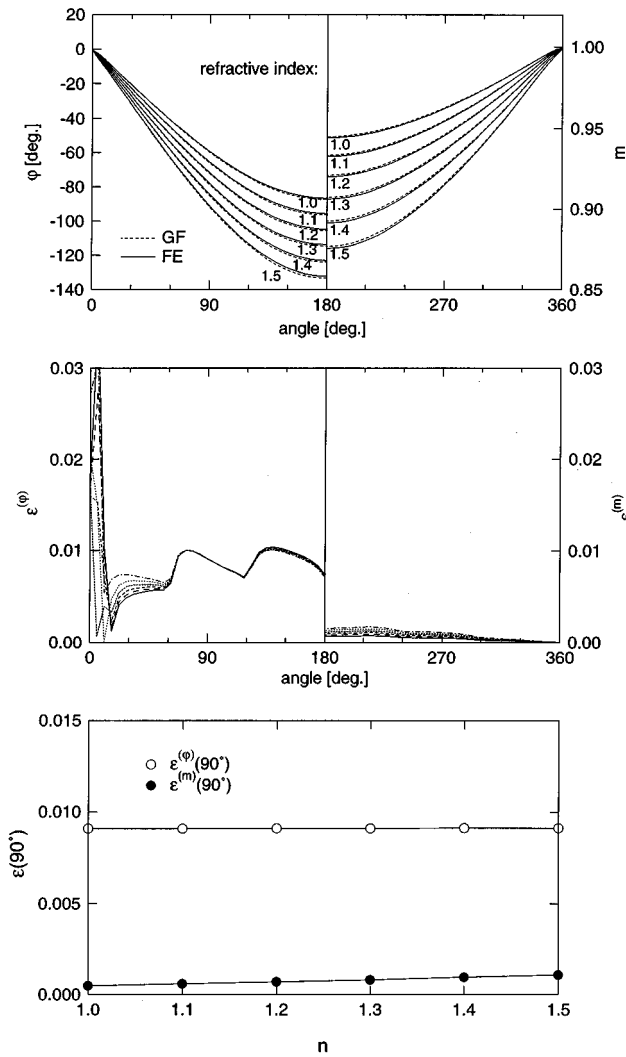


FIG. 5. Boundary measurements and FEM errors for different refractive index values. Graphs correspond to Fig. 3.

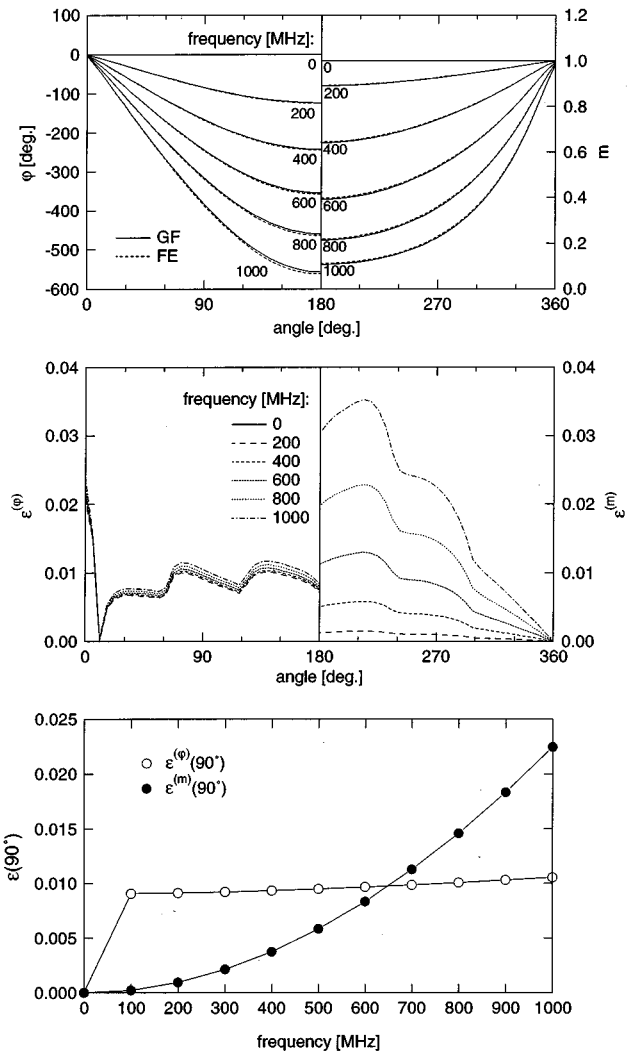


FIG. 6. Boundary measurements and FEM errors for different modulation frequencies. Graphs correspond to Fig. 3.

model depends both on the mesh resolution and on the error limit of the CG scheme, and also on the optical properties of the simulated object and the modulation frequency. An important finding is the error behavior as a function of frequency, which is strongly varying for modulation depth, but weakly for phase shift, suggesting that for modulation calculations the mesh must be carefully adjusted to the frequency used. In addition, the variation of the error with the optical properties of the object has implications for the modeling of biological tissues, which can vary considerably in its absorption and scattering properties (breast, skin, or bone tissue, white and grey brain matter, etc). For imaging applications, this may necessitate the use of iterative remeshing algorithms which adapt the FEM mesh successively to the reconstructed image.

The purpose of this paper was the rigorous evaluation of performance and error behavior of the frequency-domain FEM light transport model for a number of defined, simple cases which can be compared to analytic Green's function solutions. The analytic treatment of circular geometry with

extrapolated boundary condition [Eq. (15)] has not been reported previously. On the basis of the results it is straightforward to apply the model to more complex objects, as previously done in the time-domain case,<sup>20-24</sup> including the use of meshes derived from MRI images.<sup>25,5</sup> Interested readers can access our software for solving both the forward problem in time and frequency domain, and the inverse problem (image reconstruction) in time domain on anonymous ftp (ftp://cs.ucl.ac.uk/toast).

**ACKNOWLEDGMENT**

This work was made possible by funding from Action Research.

**APPENDIX: REVIEW OF CHOLESKY AND CONJUGATE GRADIENT METHOD**

In this section we give a brief overview of the two matrix solution techniques used in the discussed FEM model, the Cholesky and the CG method. These are standard techniques

and can be found in numerous books on numerical computation; see, e.g., Golub and van Loan<sup>18</sup> or Press *et al.*<sup>17</sup>

The Cholesky method is a direct method applicable to problems of the form

$$\mathbf{Ax}=\mathbf{b} \quad (\text{A1})$$

when  $\mathbf{A}$  is symmetric and positive definite.  $\mathbf{A}$  is decomposed into  $\mathbf{L}\cdot\mathbf{L}^T=\mathbf{A}$ , where  $\mathbf{L}$  is a lower triangular matrix.  $\mathbf{x}$  is obtained by the forward and backsubstitution  $\mathbf{Ly}=\mathbf{b}$  and  $\mathbf{L}^T\mathbf{x}=\mathbf{y}$ . The operation count for an  $n\times n$  problem is  $n^3/6$  for the decomposition and  $n^2/2$  for each forward and backsubstitution. This is about a factor of 2 better than standard Gaussian elimination. The algorithm is particularly useful where multiple right-hand sides  $\mathbf{b}$  are applied to the same matrix  $\mathbf{A}$  since the decomposition needs to be performed only once. We use the Cholesky method in the temporal-domain FEM model.<sup>6</sup>

The CG method is an iterative scheme for symmetric and positive definite problems. It seeks to minimize the functional

$$f(\mathbf{x})=\frac{1}{2}\mathbf{xAx}-\mathbf{bx} \quad (\text{A2})$$

by finding the root of the gradient  $\nabla f=\mathbf{Ax}-\mathbf{b}$ , which is equivalent to solving the original problem [Eq. (18)]. The minimization scheme iteratively constructs search directions  $\mathbf{p}_k$  and at each step coefficients  $\alpha_k$  which minimize  $f(\mathbf{x}_k+\alpha_k\mathbf{p}_k)$  where  $\mathbf{x}_k$  is the solution estimate at step  $k$ . After each step  $\mathbf{x}_k$  is updated to  $\mathbf{x}_{k+1}=\mathbf{x}_k+\alpha_k\mathbf{p}_k$ .  $\mathbf{p}_k$  and  $\mathbf{x}_k$  are constructed so that  $\mathbf{x}_{k+1}$  minimizes  $f$  over the whole vector space of all previous directions  $\mathbf{p}_1, \dots, \mathbf{p}_k$ . After  $n$  iterations the global minimum, and thus the solution  $\mathbf{x}$ , is found.

For the solution of Eq. (14) we used the biconjugate gradient method,<sup>17</sup> which is applicable to nonsymmetric matrices. Here, in each iteration step  $k$  the quantities

$$\begin{aligned} \alpha_k &= \frac{\bar{\mathbf{r}}_k \mathbf{r}_k}{\bar{\mathbf{p}}_k \mathbf{A} \mathbf{p}_k}, \\ \mathbf{r}_{k+1} &= \mathbf{r}_k - \alpha_k \mathbf{A} \mathbf{p}_k, \quad \bar{\mathbf{r}}_{k+1} = \bar{\mathbf{r}}_k - \alpha_k \mathbf{A}^T \bar{\mathbf{p}}_k, \\ \beta_k &= \frac{\bar{\mathbf{r}}_{k+1} \mathbf{r}_{k+1}}{\bar{\mathbf{r}}_k \mathbf{r}_k}, \\ \mathbf{p}_{k+1} &= \mathbf{r}_k + \beta_k \mathbf{p}_k, \quad \bar{\mathbf{p}}_{k+1} = \bar{\mathbf{r}}_k + \beta_k \bar{\mathbf{p}}_k, \\ \mathbf{x}_{k+1} &= \mathbf{x}_k + \alpha_k \mathbf{p}_k, \end{aligned} \quad (\text{A3})$$

are evaluated, starting from some initial guess  $\mathbf{x}_1$ , and  $\mathbf{r}_1 = \bar{\mathbf{r}}_1 = \mathbf{p}_1 = \bar{\mathbf{p}}_1 = \mathbf{b} - \mathbf{Ax}_1$ . In theory, when rounding errors do not occur, at most  $n$  steps are needed to arrive at the exact solution. In practical applications however the iteration is terminated as soon as a suitable error limit is reached. For the application discussed in this paper we use as the stopping criterion the normal of the residual  $\mathbf{r}$ , normalized by the right-hand side  $\mathbf{b}$ :  $\rho = |\mathbf{r}_k|/|\mathbf{b}|$ .

The rate of convergence can be improved by preconditioning  $\mathbf{A}$  to obtain a better conditioned problem, solving

$$(\tilde{\mathbf{A}}^{-1}\mathbf{A})\mathbf{x}=\tilde{\mathbf{A}}^{-1}\mathbf{b} \quad (\text{A4})$$

instead of Eq. (A1), where  $\tilde{\mathbf{A}}$  is chosen such that  $\tilde{\mathbf{A}}^{-1}\mathbf{A}\approx\mathbf{I}$ , the identity matrix. A common choice which we adopted in the FEM model is to set  $\tilde{\mathbf{A}}$  to the diagonal of  $\mathbf{A}$ ,  $\tilde{\mathbf{A}} = \text{diag}(a_{11}, \dots, a_{nn})$ .

Each iteration step requires  $14n$  operations plus two matrix-vector multiplications. The total operation count depends on the convergence rate and on the sparseness of the matrix. For the application described in this paper a matrix-vector multiplication typically requires 100n operations. We found that approximately  $\sqrt{n}$  iterations are required to achieve sufficient accuracy with the preconditioning scheme described above.

<sup>a</sup>Electronic-mail: martins@medphys.ucl.ac.uk

<sup>1</sup>S. R. Arridge, M. Cope, and D. T. Delpy, "Theoretical basis for the determination of optical pathlengths in tissue: Temporal and frequency analysis," *Phys. Med. Biol.* **37**, 1531–1560 (1992).

<sup>2</sup>D. T. Delpy, M. Cope, P. van der Zee, S. R. Arridge, S. Wray, and J. Wyatt, "Estimation of optical pathlength through tissue from direct time of flight measurement," *Phys. Med. Biol.* **33**, 1433–1442 (1988).

<sup>3</sup>A. Duncan, T. L. Whitlock, M. Cope, and D. T. Delpy, "A multiwavelength, wideband, intensity modulated optical spectrometer for near infrared spectroscopy and imaging," *Proc. SPIE* **1888**, 248–257 (1993).

<sup>4</sup>M. Kaschke, H. Jess, G. Gaida, J. Kaltenbach, and W. Wrobel, "Transillumination imaging of tissue by phase modulation techniques," in *Advances in Optical Imaging and Photon Migration*, edited by R. Alfano [Proc. OSA **21**, 88–92 (1994)].

<sup>5</sup>S. R. Arridge and M. Schweiger, "Photon measurement density functions. 2. Finite element calculations," *Appl. Opt.* **34**, 8026–8037 (1995).

<sup>6</sup>S. R. Arridge, M. Schweiger, M. Hiraoka, and D. T. Delpy, "A finite element approach for modeling photon transport in tissue," *Med. Phys.* **20**, 299–309 (1993).

<sup>7</sup>S. R. Arridge and M. Schweiger, "Direct calculation of the moments of the distribution of photon time of flight in tissue with a finite-element method," *Appl. Opt.* **34**, 2683–2687 (1995).

<sup>8</sup>B. W. Pogue and M. S. Patterson, "Frequency-domain optical absorption spectroscopy of finite tissue volumes using diffusion theory," *Phys. Med. Biol.* **39**, 1157–1180 (1994).

<sup>9</sup>J. L. Karagiannes, Z. Zhang, B. Grossweiner, and L. I. Grossweiner, "Applications of the 1D diffusion approximation to the optics of tissues and tissue phantoms," *Appl. Opt.* **28**, 2311–2317 (1989).

<sup>10</sup>J. P. Kaltenbach and M. Kaschke, "Frequency- and time-domain modeling of light transport in random media," in *Medical Optical Tomography: Functional Imaging and Monitoring*, edited by G. Muller *et al.* (SPIE, Bellingham, WA, 1993), pp. 65–86.

<sup>11</sup>T. J. Farrell and M. S. Patterson, "A diffusion theory model of spatially resolved, steady-state diffuse reflectance for the noninvasive determination of tissue optical properties *in vivo*," *Med. Phys.* **19**, 879–888 (1992).

<sup>12</sup>M. S. Patterson, S. Anderson-Engels, B. C. Wilson, and E. K. Osei, "Absorption spectroscopy in tissue-simulating materials: A theoretical and experimental study of photon paths," *Appl. Opt.* **34**, 22–30 (1995).

<sup>13</sup>M. Schweiger, S. R. Arridge, M. Hiraoka, and D. T. Delpy, "The finite element model for the propagation of light in scattering media: Boundary and source conditions," *Med. Phys.* **22**, 1779–1792 (1995).

<sup>14</sup>G. Eason, A. R. Veitch, R. M. Nisbet, and F. W. Turnbull, "The theory of backscattering of light by blood," *J. Phys. D Appl. Phys.* **11**, 1463–1479 (1978).

<sup>15</sup>J. D. Moulton, "Diffusion modelling of picosecond laser pulse propagation in turbid media," M. Eng. thesis, McMaster University, Hamilton, Ontario, 1990.

<sup>16</sup>M. Keijzer, W. M. Star, and P. R. M. Storchi, "Optical diffusion in layered media," *Appl. Opt.* **27**, 1820–1824 (1988).

<sup>17</sup>W. H. Press, S. A. Teukolsky, W. T. Vetterling, and B. P. Flannery, *Numerical Recipes in C*, 2nd ed. (Cambridge University Press, Cambridge, 1992).

<sup>18</sup>G. H. Golub and C. F. van Loan, *Matrix Computations* (Johns Hopkins University, Baltimore, Maryland, 1983).

<sup>19</sup>M. Schweiger, "Application of the Finite Element Method in Infrared

- Image Reconstruction of Scattering Media," Ph.D. thesis, University of London, 1994.
- <sup>20</sup>M. Schweiger, S. R. Arridge, H. Hiraoka, and D. T. Delpy, "Application of the finite element method for the forward model in infrared absorption imaging," *Proc. SPIE* **1768**, 97–108 (1992).
- <sup>21</sup>M. Schweiger, S. R. Arridge, and D. T. Delpy, "Application of the finite-element method for the forward and inverse models in optical tomography," *J. Math. Imag. Vision* **3**, 263–283 (1993).
- <sup>22</sup>M. Schweiger, S. R. Arridge, H. Hiraoka, M. Firbank, and D. T. Delpy, "Comparison of a finite element forward model with experimental phantom results: Application to image reconstruction," *Proc. SPIE* **1888**, 179–190 (1993).
- <sup>23</sup>E. Okada, M. Schweiger, S. R. Arridge, M. Firbank, and D. T. Delpy, "Experimental validation of Monte Carlo and finite-element methods for the estimation of the optical path length in inhomogeneous tissue," *Appl. Opt.* **35**, 3362–3371 (1996).
- <sup>24</sup>E. Okada, M. Firbank, M. Schweiger, S. R. Arridge, and D. T. Delpy, "Analysis of light propagation in inhomogeneous turbid media by time-resolved measurement," *Jpn. J. Opt.* **25**, 33–41 (1996).
- <sup>25</sup>S. R. Arridge and M. Schweiger, "Sensitivity to prior knowledge in optical tomographic reconstruction," in *Optical Tomography, Photon Migration, and Spectroscopy of Tissue and Model Media: Theory, Human Studies, and Instrumentation*, edited by B. Chance and R. R. Alfano [Proc. SPIE **2389**, 378–388 (1995)].